Geophysical Journal International

Geophys. J. Int. (2025) **243,** 1–16
Advance Access publication 2025 July 29
Seismology

https://doi.org/10.1093/gji/ggaf289

Crustal rheological characteristics in the Scandinavian Peninsula and its vicinity implied from *Lg*-wave attenuation tomography

Zhen Liu,[1,2] Lian-Feng Zhao ,[1,3] Xiao-Bi Xie,[4] Baofeng Tian[5] and Zhen-Xing Yao[1]

[1]*Key Laboratory of Earth and Planetary Physics, Institute of Geology and Geophysics, Institute of Geology and Geophysics, Chinese Academy of Sciences, Beijing* 100029*, China. E-mail: zhaolf@mail.iggcas.ac.cn*
[2]*College of Earth and Planetary Sciences, University of Chinese Academy of Sciences, Beijing* 100049*, China*
[3]*Heilongjiang Mohe National Observatory of Geophysics, Institute of Geology and Geophysics, Chinese Academy of Sciences, Beijing* 165303*, China*
[4]*Institute of Geophysics and Planetary Physics, University of California at Santa Cruz, Santa Cruz, CA* 95064*, USA*
[5]*Institute of Geophysics, China Earthquake Administration, Beijing* 100081*, China*

Accepted 2025 July 25. Received 2025 July 15; in original form 2024 October 14

SUMMARY

The Scandinavian Peninsula and its vicinity comprise highly tectonically diverse blocks, including the Baltic Shield, the continental margin and the North Sea Basin. The crustal rheology is a critical constraint to understanding the tectonic evolution in this region. Based on 19 416 *Lg* waveforms from 233 earthquakes and 560 broad-band digital stations, using an inversion method combining both single- and two-station ray paths, we constructed a broad-band (0.05 and 10.0 Hz) *Lg*-wave attenuation model in the study region, with the resolution approaches to 110 km (∼1°) or higher in areas with dense ray path coverages. The Q_{Lg} distributions correlate well with regional geological features. The Baltic Shield exhibits the highest Q_{Lg}, consistent with its thick Precambrian crust and high-rheological rigidity developed through Archean Svecofennian orogeny. In contrast, passive margins with crustal thinning, magmatic modification, and thick sedimentary sequences exhibit strong attenuation, reflecting a reduction in rheological strength resulting from interactions with mantle plumes and extensional tectonics. The North Sea Basin exhibits the lowest Q_{Lg} values and the presence of hydrocarbon-bearing sediments. The extremely high Q_{Lg} distribution reveals the ancient cratonic core of the Baltic Shield, particularly in areas where the surface rock dating sample cannot be collected due to sea water coverage.

Key words: Europe; Seismic attenuation; Seismic tomography; Crustal structure; Rheology: crust and lithosphere.

1 INTRODUCTION

The Scandinavian Peninsula, situated northwest of the European continent, is the largest in Europe, spanning approximately 1850 km in length. It is adjacent to the North Atlantic Ocean and borders the Norwegian Sea to the west, the Baltic Sea to the east, and the North Sea to the south (Fig. 1). The oceanic crust of the North Atlantic Ocean is connected to the European continent by a series of passive continental margins, mainly including the Lofoten–Vesterålen margin, the Vøring margin and the Møre margin. The divisions between these three margins are the Bivrost Fracture Zone and the Jan Mayen Fracture Zone (Ziegler 1986). This continental margin underwent continental rifting from the Carboniferous to the Early Cretaceous period. The continental rifting and seafloor spreading effects in the North Atlantic, from the Late Cretaceous to the Early Eocene, and their associated extensional tectonics were influenced by the relative motion of the plate boundaries, locally exhibiting a pronounced extrusion structure (Bukovics *et al.* 1984; Blystad *et al.* 1995; Bogdanova *et al.* 2008).

The basement of the Lofoten–Vesterålen margin is characterized by asymmetric half-graben tectonics and thick sediments (Blystad *et al.* 1995; Faleide *et al.* 2008). The Vøring margin features anomalously thick oceanic crust, overlain by early Eocene basalts, and continental crust, overlain by thick Cretaceous sediments (Mjelde 2005; Tsikalas *et al.* 2005). The crystalline basement of the Møre margin thins rapidly from more than 25 km thick at the coast to less than 10 km thick in the continental–marine transition zone, characterized by igneous intrusions in the bedrock and an unconsolidated sedimentary cover (Mosar 2003; Mjelde 2005; Kvarven *et al.* 2016).

The Baltic Shield, which formed at approximately 3.5–1.5 Ga, belongs to the Eastern European Craton and has the oldest lithosphere in the European continent and a thickness of 250–300 km (Gaál & Gorbatschev 1987; Lahtinen *et al.* 2008; Pedersen *et al.* 2013). The North Sea Basin in the south is primarily composed of the Viking

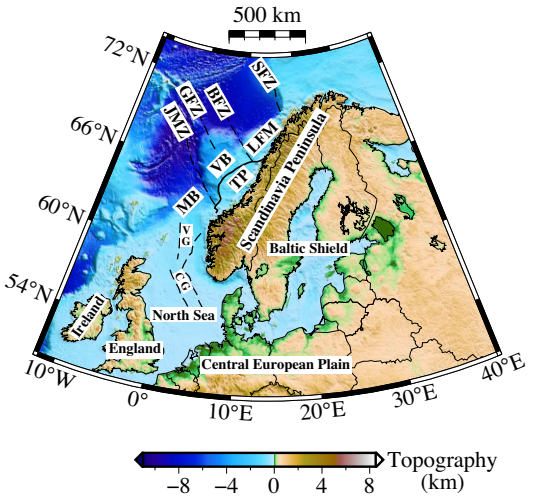

Figure 1. Surface topography of the Scandinavian Peninsula and surrounding areas. Structural elements are adopted after Mosar (2003): VB: Vøring Basin; LFM: Lofoten–Vesterålen Margin; MB: Møre Basin; TP: Trøndelag Platform; VG: Viking Graben; CG: Central Graben; JMZ, GFZ, BFZ, SFZ: Jan Mayen, Gleipne, Bivrost, Senja Fracture Zones.

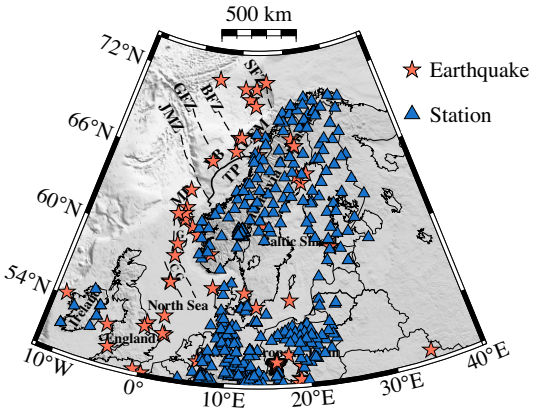

Figure 2. Distributions of selected earthquakes (pentagons) and stations (triangles) used in this study.

Graben and the Central Graben, which run nearly north–south and are characterized by large rotational fault blocks with accompanying sedimentary cover. These grabens are associated with lithospheric extension and crustal thinning, with the Central Graben also influenced by salt dynamics (Sclater & Christie 1980). These structures form a long, active and weak zone inherited from the Caledonian orogeny, playing a crucial role in the later evolution of the North Sea Basin (Faleide *et al.* 2010).

Scandinavia and the surrounding area, where three crustal structure types are distributed, is an ideal region to study the characteristics of crustal attenuation. However, in recent years, only sporadic studies of crustal *Lg*-wave attenuation features have been carried out on peninsulas and continental margins, and more recent data need to be incorporated to explore high-resolution crustal attenuation structures in and around Scandinavia.

Seismic *Lg* waves are a stable phase on high-frequency seismograms observed in continental regions (e.g. Gutenberg 1955). *Lg* waves are generally considered to be formed by the superimposition of higher-order surface waves or multiple supercritical reflection shear waves occurring in crustal waveguides (Gutenberg 1955; Knopoff *et al.* 1973; Bouchon 1982; Hasegawa 1985; Kennett 1986; Xie & Lay 1994). *Lg* waves, which mainly propagate in the crust, are often used to investigate source parameters, the crustal attenuation structure, and site responses (Aki & Chouet 1975; Singh & Herrmann 1983; Campillo & Plantet 1991; Yoshimoto *et al.* 1993; Ottemöller *et al.* 2002; Zhao *et al.* 2010). The quality factor, Q_{Lg}, one of the parameters characterizing the crust, is often used to describe the attenuation of *Lg* waves. Q_{Lg} is affected by rock type, crustal thermal state and inhomogeneity. Hence, *Lg* wave amplitude attenuation is also closely related to the properties of the crustal medium, fluid content, crustal thickness variation and crustal geological structure (Bouchon 1982; Furumura & Kennett 1997). Low Q values and strong attenuation are typically observed in recently deformed crust and active tectonic environments, while high Q values and weak attenuation are observed in stable tectonic environments (Singh & Herrmann 1983; Wu *et al.* 2000; Fan & Lay 2003; Erickson *et al.* 2004; Xie *et al.* 2006; He *et al.* 2021). *Lg* waves may be blocked or strongly attenuated as they propagate through earthquake-prone areas with strong variations in the crustal structure, partial melting zones, high-temperature anomalies, oceanic crust, thin continental crust and areas with thick sedimentary cover (Press & Ewing 1952; Ruzaikin *et al.* 1977; Campillo *et al.* 1993; Shapiro *et al.* 1996; Zor *et al.* 2007; Pasyanos *et al.* 2009; Zhao *et al.* 2013a; Zhao & Xie 2016; Zhang *et al.* 2022). Hence, to explore the attenuation features of different crustal structures, we utilize more extensive and recent *Lg* wave data to construct a high-resolution broad-band attenuation model in Scandinavia and its surrounding areas.

2 DATA

2.1. Regional seismic data

We collected 19 416 vertical-component waveforms from 233 earthquakes in the Scandinavian Peninsula and adjacent regions between 2007 and 2024, recorded by 560 broad-band digital seismic stations. These data were obtained from the Incorporated Research Institutions for Seismology (IRIS) website and the GEOFON data centre (Tables S1–S3, Supporting Information). The *Lg* waveforms with epicentre distances between 200 and 3000 km were selected to form the *Lg* wave data set (Zhao *et al.* 2013a, b, 2010). The focal depths are shallower than the Moho depth given by CRUST1.0 (Laske *et al.* 2013). To ensure a good signal-to-noise ratio (SNR) and avoid the impacts of the complex rupture processes associated with large earthquakes, we selected events with magnitudes ranging from 4.0 to 6.5 in the continental environment and from 5.0 to 6.5 in the marine environment, respectively. Only stations that recorded at least three events and events recorded by at least three stations were used. Fig. 2 shows the distributions of earthquakes and stations used in this study. These sources and stations provided dense ray coverage for the study area.

2.2. *Lg* wave amplitude spectrum

Following Zhao *et al.* (2010, 2013b), the *Lg* waveforms are obtained from vertical-component seismograms with the instrument responses removed. The *Lg*-wave group velocity is approximately 3.5 km s^{-1} (Fig. 3) (Zhao & Xie 2016). However, considering potential impacts from factors such as the origin time, epicentre location, source depth and the regional variations of *Lg*-wave group velocities, we adopted a moving group velocity window obtained by

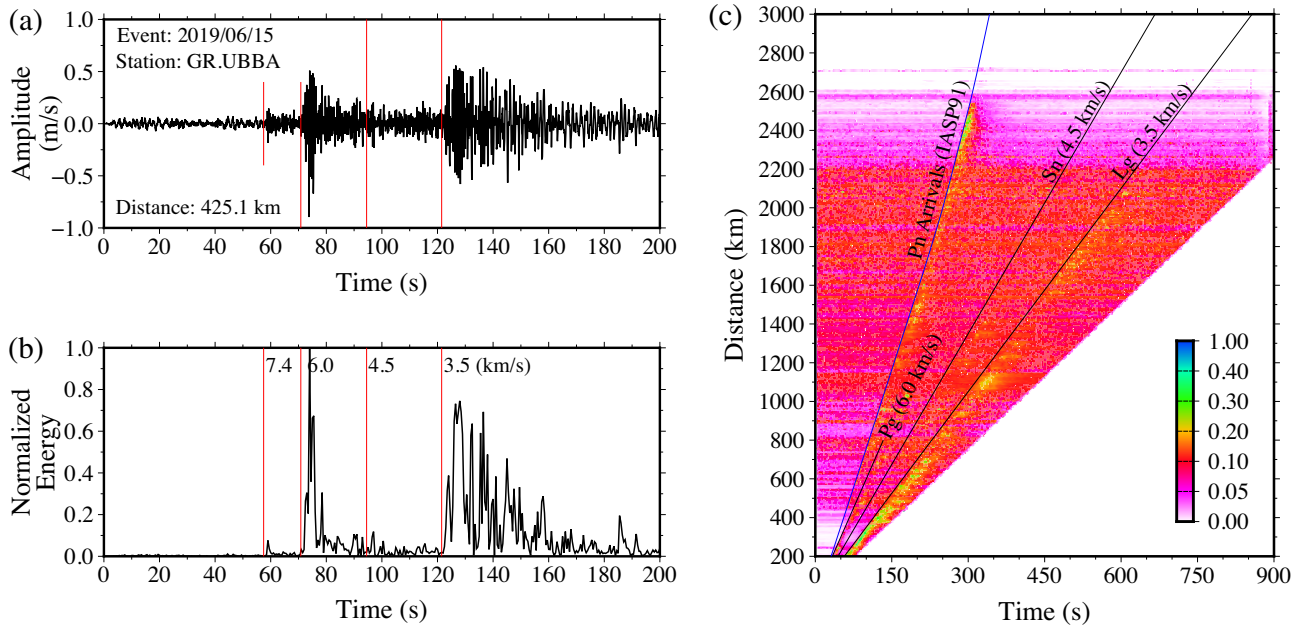

Figure 3. (a) Sample seismogram from an earthquake that occurred on 2019/06/15 and recorded by station GR.UBBA, (b) its normalized energy and (c) the record section of normalized energy for all seismic phases used in this study. The colour bar illustrates the energy level. The regional phases Pn, Sn, and Lg, along with their typical group velocities, are labelled in panel (c).

sliding a 0.6 km s^{-1} long velocity window between group velocities 3.7 and 2.8 km s^{-1}, and choosing the window which outputs the maximum energy as the *Lg*-wave group velocity window to sample the *Lg* wave signal (Zhao & Xie 2016). The pre-P and the pre-Lg noise series were obtained from time windows with the same length as the *Lg* waveform for noise analysis. The *Lg*-wave, pre-P and pre-Lg noise amplitude spectra were calculated using the Fast Fourier Transform at 58 discrete frequencies log-evenly distributed between 0.05 and 10.0 Hz. The SNR between the *Lg* signal, pre-P and pre-Lg noise were calculated and used to eliminate low-quality data. To ensure data quality, an SNR threshold of 2.0 is employed (e.g. Luo *et al.* 2021). The *Lg*-wave amplitude was corrected for the noise by using $A_s^2(f) = A_O^2(f) - A_N^2(f)$, where A denotes the amplitude spectrum, f is the frequency, A_s, A_O and A_N represent true signal amplitude, observed amplitude of the *Lg*-wave, and noise amplitude, respectively. In this correction, we assumed that the observed waveform is composed of both the *Lg* signal and the noise, which are uncorrelated (Schlittenhardt 2001; Zhao *et al.* 2010, 2013a). Fig. 4 illustrates the process of *Lg*-wave amplitude measurement for an earthquake. Based on this procedure, a high-quality *Lg*-wave spectral data set was obtained for our *Lg*-wave Q tomography.

3 METHODS

3.1. Modelling of the *Lg* amplitudes

The *Lg*-wave amplitude spectrum can be modelled by (Sato 1967)

$$A(f, \Delta) = S(f)\, G(\Delta)\, \Gamma(f, \Delta)\, P(f) r(f), \tag{1}$$

where $A(f, \Delta)$ is the *Lg* wave amplitude at the frequency f and at the epicentral distance Δ, $S(f)$ is the source spectrum, $G(\Delta)$ is the geometrical spreading function, $\Gamma(f, \Delta)$ is the attenuation function, $P(f)$ is the site response function and $r(f)$ is a random factor composed of unknown errors. $S(f)$ can be expressed as (Street *et al.* 1975)

$$S(f) = \frac{M_0 R}{4\pi\rho v_s^3} \cdot \frac{1}{1 + \frac{f}{f_c}}, \tag{2}$$

where M_0 is the scalar seismic moment, ρ and v_s are the density and shear wave velocity in the source region, f_c is the corner frequency and R is the source radiation pattern. Since *Lg* wave has relatively wide incidence angles, its radiation can be assumed isotropic (Castro *et al.* 1990; Zhao & Mousavi 2018). $G(\Delta)$ usually can be expressed as (Street *et al.* 1975; Herrmann & Kijko 1983)

$$G(\Delta) = (\Delta\Delta_0)^{-\frac{1}{2}}, \tag{3}$$

where Δ_0 is a reference distance which can take 100 km. $\Gamma(f, \Delta)$ can be expressed as (e.g. Zhao *et al.* 2010)

$$\Gamma(f, \Delta) = \exp\left(\frac{-\pi f}{v} \int_{\text{event}}^{\text{station}} \frac{\mathrm{d}s}{Q(x, y, f)}\right), \tag{4}$$

where v represents the *Lg*-wave group velocity, $Q(x, y, f)$ is the *Lg*-wave quality factor and is a function of surface location (x, y) and frequency f, and $\int_{\text{event}}^{\text{station}} \mathrm{d}s$ represents an integration from the source to station along the great circle path. Thus, as a function of frequency f, the *Lg*-wave spectral amplitude A_{kj} from event k recorded at station j can be expressed as (Fig. 5a)

$$A_{kj} = S_k G_{kj} \Gamma_{kj} P_j r_{kj} = \left(\frac{M_0 R}{4\pi\rho v_s^3} \cdot \frac{1}{1 + \frac{f}{f_c}}\right) \cdot \left[(\Delta_{kj}\Delta_0)^{-\frac{1}{2}}\right] \cdot \left[\exp\left(\frac{-\pi f}{v} \int_k^j \frac{\mathrm{d}s}{Q(x, y, f)}\right)\right] \cdot P_j r_{kj}. \tag{5}$$

If earthquake k is simultaneously recorded by two stations i and j, and the epicentre and two stations are located on the same great circle (Fig. 5b), two-station data can be constructed by calculating

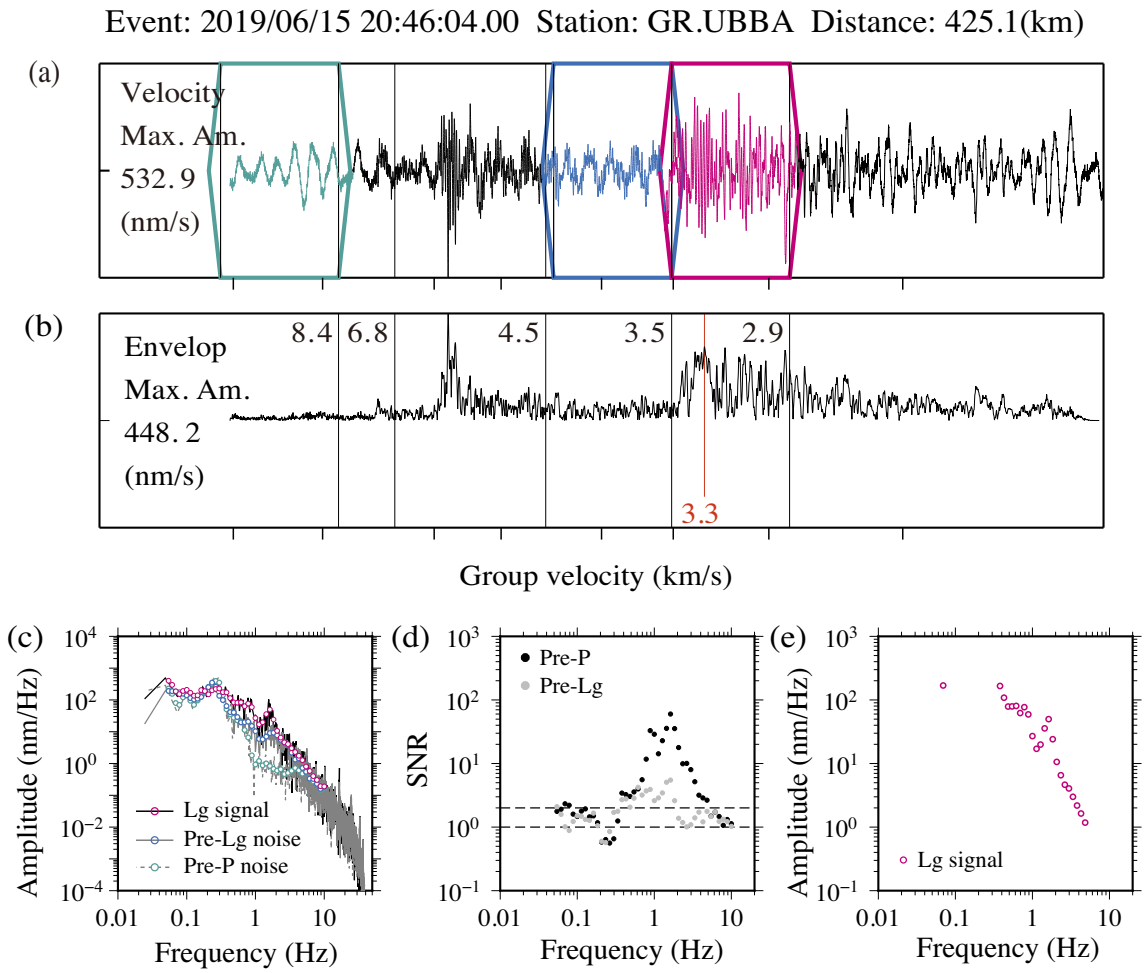

Figure 4. Example of *Lg*-wave amplitude spectrum measurement. (a) Velocity waveforms bandpass filtered between 0.5 and 5.0 Hz from an event that occurred on 2019/06/15 and was recorded by station GR.UBBA. The rose pink, blue and green windows sample the *Lg* signal, pre-Lg and pre-P noise. (b) Envelope of 0.5–5.0 Hz filtered waveform for locating the maximum energy arrival and Lg sampling window. (c) Amplitude spectra of the *Lg* wave, pre-Lg and pre-P noise, where the black solid, grey solid and grey dotted lines represent the original amplitude spectra, and the rose pink, blue and green circles denote amplitude spectra at discrete frequencies. (d) Signal-to-noise ratio (SNR). (e) The *Lg*-wave amplitude spectrum after noise correction, and data points with SNR below the thresholds, were discarded.

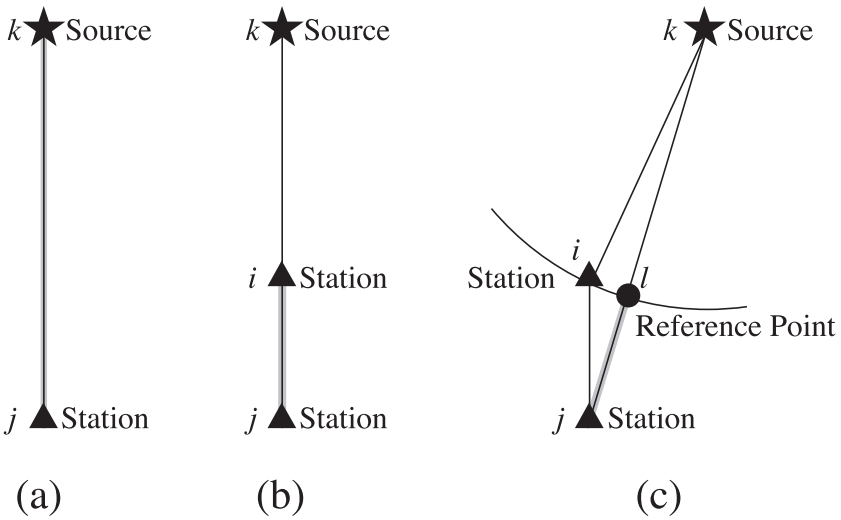

Figure 5. Distribution of source-station geometry. (a) Geometry of single-station data, (b) geometry for the original two-station data and (c) revised two-station geometry. To make the approximation valid, the distance between locations i and l is required to be smaller than half of the interval of the inversion grid.

their *Lg*-wave spectral amplitude ratios (e.g. Zhao *et al.* 2013a):

$$A_{ij} = \frac{A_{kj}}{A_{ki}} = \left(\frac{\Delta_{kj}}{\Delta_{ki}}\right)^{-\frac{1}{2}} \cdot \exp\left(\frac{-\pi f}{v} \int_i^j \frac{\mathrm{d}s}{Q(x,y,f)}\right) \cdot \frac{P_j}{P_i} \cdot \frac{r_{kj}}{r_{ki}}, \tag{6}$$

where A_{kj} and A_{ki} are *Lg*-wave spectral amplitudes recorded by stations j and i from event k, Δ_{kj} and Δ_{ki} are epicentral distances from event k to stations j and i, P_j and P_i are site responses at stations j and i, r_{kj} and r_{ki} are random errors in the related propagation path. The two-station data shown in eq. (6) can effectively reduce the compromise between attenuation and source spectrum (Xie *et al.* 2004). However, the actual locations of the two stations are hardly exactly on the same great circle path. To increase the available data, the great circle path requirement can be appropriately relaxed. Fig. 5 illustrates the geometry of the source and stations, where 5(a) is for single-station data and 5(b) is the great circle geometry for two-station data. As shown in Fig. 5(c), to include stations slightly biased from the great circle geometry, a reference point l is set on the path from event k to station j (Zhao *et al.* 2013b). Letting the distance from the event k to reference point l equal that from k to station i and requiring the distance between points i and l less than half the interval of the tomographic grid, the *Lg* wave amplitude at the reference point l can be approximated by that observed at station i. In this way, we can largely increase the available two-station data without losing the accuracy. The revised two-station data can be expressed as:

$$A_{lj} = \frac{A_{kj}}{A_{ki}} \approx \left(\frac{\Delta_{kj}}{\Delta_{kl}}\right)^{-\frac{1}{2}} \cdot \exp\left(\frac{-\pi f}{v} \int_l^j \frac{\mathrm{d}s}{Q(x,y,f)}\right) \cdot \frac{P_j}{P_i} \cdot \frac{r_{kj}}{r_{ki}}. \tag{7}$$

3.2. Q_{Lg} tomography

Following Zhao *et al.* (2010, 2013b), and we established a linear system for *Lg* wave Q tomography. By substituting eq. (4) into eq. (1), taking natural logarithms for both sides, and ignoring the random term, we obtain:

$$\ln[A(f,\Delta)] = \ln[S(f)] + \ln[G(\Delta)] - \frac{\pi f}{v} \int_{\text{event}}^{\text{station}} \frac{\mathrm{d}s}{Q(x,y,f)} + \ln[P(f)]. \tag{8}$$

To solve the above equation in an iterative way, the perturbation method is used. Assuming the attenuation, source function and site response can be expressed as their initial values Q^0, S^0 and P^0 and perturbations

$$\frac{1}{Q(x,y,f)} \approx \frac{1}{Q^0(x,y,f)} - \frac{\delta Q(x,y,f)}{\left[Q^0(x,y,f)\right]^2}, \tag{9}$$

$$ln[S(f)] = ln\left[S^0(f)\right] + \delta ln[S(f)], \tag{10}$$

$$ln[P(f)] = ln\left[P^0(f)\right] + \delta ln[P(f)]. \tag{11}$$

Substituting eqs (9)–(11) into eq. (8), we have

$$\ln[A(f,\Delta)] = \ln\left[A^0(f,\Delta)\right] + \delta\ln[S(f)] + \frac{\pi f}{v} \int_{\text{event}}^{\text{station}} \frac{\delta Q(x,y,f)}{\left[Q^0(x,y,f)\right]^2}\mathrm{d}s + \delta\ln[P(f)], \tag{12}$$

where

$$\ln\left[A^0(f,\Delta)\right] = \ln\left[S^0(f)\right] + \ln[G(\Delta)] - \frac{\pi f}{v} \int_{\text{event}}^{\text{station}} \frac{\mathrm{d}s}{Q(x,y,f)} + \ln\left[P^0(f)\right]. \tag{13}$$

The perturbation of the amplitude spectrum can be expressed by:

$$\delta\ln[A(f,\Delta)] = \ln[A(f,\Delta)] - \ln\left[A^0(f,\Delta)\right]. \tag{14}$$

Substituting eqs (12)–(13) into eq. (14), we obtain:

$$\delta\ln[A(f,\Delta)] = \delta\ln[S(f)] + \frac{\pi f}{v} \int_{\text{event}}^{\text{station}} \frac{\delta Q(x,y,f)}{\left[Q^0(x,y,f)\right]^2} ds + \delta\ln[P(f)]. \tag{15}$$

We denote the amplitude residual $\delta ln[A_{ki}(f,\Delta)]$ of event k recorded by station i at frequency f as $\tilde{h}_{ki}(f)$, and decompose it onto the path based on a discretized grid

$$\tilde{h}_{ki}(f) = \sum_{m=1}^{M} (a_{im}.\delta Q_m) + e_k \cdot \delta\ln[S_k(f)] + u_i \cdot \delta\ln[P_i(f)], \tag{16}$$

where M is the total number of grids in the tomographic model, m is the index of a grid point, the coefficient matrix $a_{im} = \frac{\pi f}{v}\frac{D_m}{(Q^0(x_m,y_m,f))^2}$, (x_m, y_m) is the location of grid m, and D_m denotes the length of a ray section in grid m and e_j and u_i are coefficients of the site response and the source function, respectively. For single-station data, $e_k = u_i = 1$. Hence, the matrix equation for updating the *Lg*-wave Q perturbation from the single-station data is

$$H_{1sta} = A_{1sta}.\delta Q + E_{1sta}.\delta S + U_{1sta}.\delta P. \tag{17}$$

where H_{1sta} is a vector composed of the residual between the observed amplitude and the theoretical amplitude, δQ is the correction value of the Q value to be calculated, δS and δP are the correction values of the source term and the site term, A_{1sta}, E_{1sta} and U_{1sta} are the corresponding coefficient matrices. Since the source term is eliminated when using the two-station data, the matrix equation becomes:

$$H_{2sta} = A_{2sta} \cdot \delta Q + U_{2sta} \cdot \delta P. \tag{18}$$

It is generally assumed that $\sum_{i=1}^{M} \delta ln[P_i(f)] = 0$ (Ottemöller *et al.* 2002; Zhao & Mousavi 2018), thus the site response term δP is commonly ignored in the inversion (e.g. Zhang *et al.* 2022; Yang *et al.* 2023). Combining eqs (17) and (18), we established a joint inversion system for both the *Lg* wave Q value and source function based on single- and two-station data

$$\begin{bmatrix} H_{1sta} \\ H_{2sta} \end{bmatrix} = \begin{bmatrix} A_{1sta} \\ A_{2sta} \end{bmatrix} \cdot \delta Q + \begin{bmatrix} E_{1sta} \\ 0 \end{bmatrix} \cdot \delta S. \tag{19}$$

The least-squares QR factorization algorithm (Paige & Saunders 1982) was used to solve eq. (19) to obtain the perturbations of both attenuations and source functions. These perturbations are then used to update the initial or intermediate values and enter the next iteration until the optimal solution is reached. For initial Q values, we use the regional average Q model obtained from the two-station data (e.g. Ma *et al.* 2023). To reach the convergence, we minimize the L2 norm between the observed and predicted *Lg*-wave amplitude spectra (Zhao *et al.* 2010, 2013b). Fig. 6 demonstrates the distributions of residuals before and after the inversion at selected frequencies, where the residuals after the inversion tend to be Gaussian distributed, with near-zero means and much smaller standard deviations. The remaining residuals may result from complex source processes, site responses and other random effects (Zhao & Mousavi 2018). Finally, we obtain the *Lg*-wave Q distributions and source functions at 58 independent frequencies between 0.05 and 10.0 Hz.

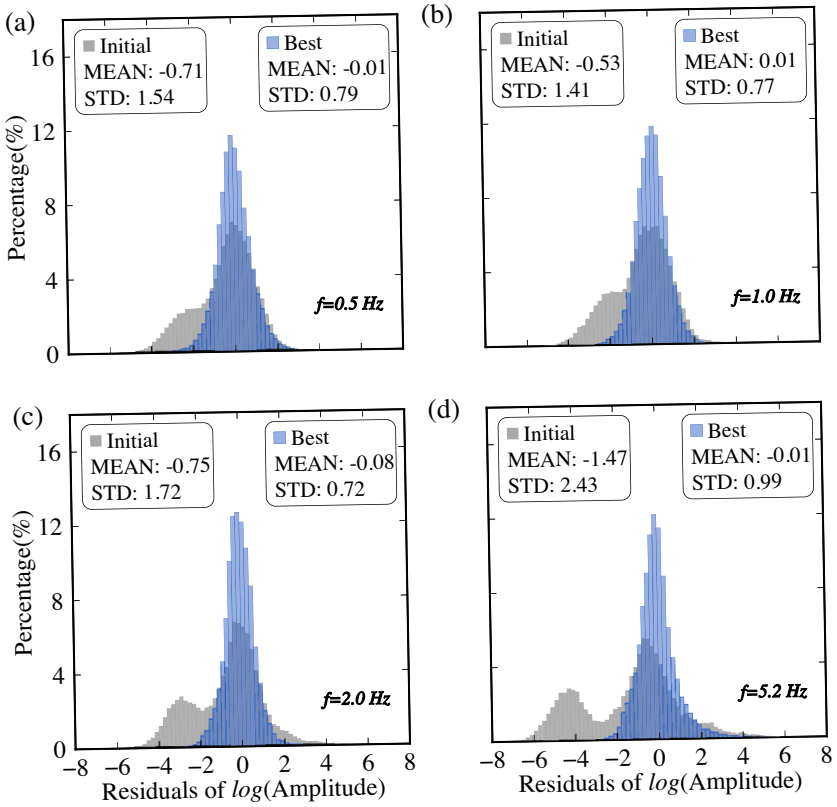

Figure 6. (a–d) Histograms of the *Lg* spectral amplitude misfits before (solid gray) and after (open blue) inversion at frequencies 0.5, 1.0, 2.0 and 5.2 Hz, respectively. The post-inversion errors tend to be Gaussian distributed with zero means and much small standard deviations, indicating much improved fitting to the data.

3.3. Resolution test

The checkerboard method is used to analyse the spatial resolution of the *Lg*-wave Q tomography (e.g. Zhao *et al.* 2013b). The testing model consists of a constant background Q, superimposed with ±7 per cent checkerboard-shaped Q perturbations (Zelt 1998; Zhou *et al.* 2011; Zhao *et al.* 2013a). To consist of the source and station locations and ray path coverage in the real data, the *Lg*-wave amplitudes are synthesized using eq. (1), and 7 per cent root-mean-square random perturbations are added to the synthetic amplitudes to simulate the real noise. These synthetic *Lg*-wave spectra, including single- and two-station data, were used to reconstruct the checkerboard model based on our *Lg*-wave Q tomography method. The resolutions are frequency-dependent because the ray coverage and the SNR differ at different frequencies (Fig. 7). Therefore, we conducted resolution analyses at all 58 independent frequencies using the checkerboard models of 110 × 110 km^2 (∼1° × 1°) (Fig. 8). The station and earthquake distributions lead to regional variations in resolution. The targeted main tectonic blocks, such as the Baltic Shield, passive continental margin, and North Sea basin, have dense ray coverage and relatively high-spatial resolutions of up to 110 km (∼1°) (Fig. 8), apparently higher than previous studies in this region (Demuth *et al.* 2019).

To overcome the difficulty caused by spherical coordinates at high-latitude areas, the tomography was performed using geodetic coordinates interpolated directly with the GMT (Generic Mapping Tool) mapproject (Smith & Wessel 1990; Wessel *et al.* 2019). The resolution tests were obtained using the same strategy.

4 RESULTS

4.1. Q_{Lg} maps at individual frequencies

The resulting attenuation model comprises Q_{Lg} distributions at 58 individual frequencies between 0.05 and 10.0 Hz. Illustrated in Figs 9(a)–(c) are Q_{Lg} maps at 1.0, 2.0 and 5.2 Hz, respectively. The most prominent feature of these Q_{Lg} maps is that the high-frequency Q_{Lg} is generally higher than that at lower frequencies. The lateral Q_{Lg} variations are consistent with regional tectonics. The Scandinavian Peninsula, mainly controlled by the shield structure and dominated by the Baltic Shield, formed in the Precambrian, is a typical craton and shield region characterized by high Q_{Lg} (Pedersen *et al.* 2013). Relatively strong attenuation and low-Q_{Lg} anomalies can be observed in the passive continental margins on the western side of Scandinavia. The thick sediments and thin crust (Figs 9d–e) may lead to these low-Q_{Lg} anomalies (Tesauro *et al.* 2008; Artemieva & Thybo 2013; Artemieva & Shulgin 2019). Strong low-Q_{Lg} anomalies were observed in the North Sea basin in southern Scandinavia. Based on regional geology, it is speculated that the overlying thick sediments or developed graben structures block the propagation of *Lg* waves (Kennett & Mykkeltveit 1984; Mendi *et al.* 1997). Our Q_{Lg} model is consistent with previous results (Demuth *et al.* 2019), but it has relatively higher resolution.

4.2. Broad-band Q_{Lg} images

Lg-wave attenuation tomography was carried out independently at individual frequencies, without any *a priori* assumptions

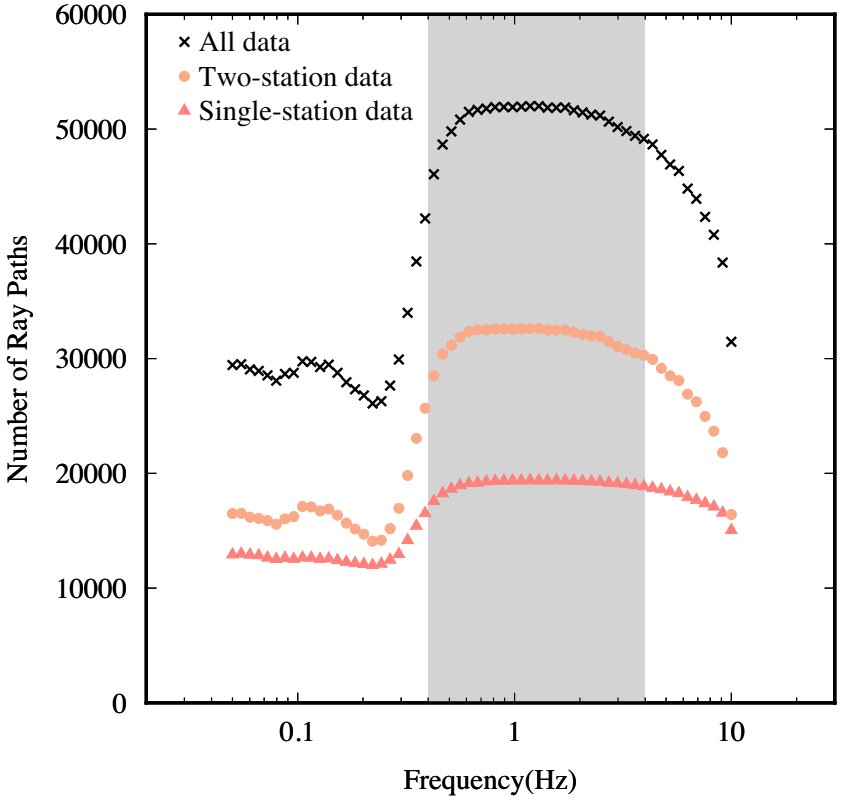

Figure 7. Ray numbers versus the frequency for the single-station, two-station and combined single and two-station data. High-ray numbers are between 0.4 and 4.0 Hz (shaded area). Therefore, at these frequencies, resolutions of approximately 110 km (∼1°) can be achieved.

regarding the relationship between Q_{Lg} and frequency, and therefore, the resulting tomographic model can be utilized to investigate the frequency dependence of Q_{Lg} further (; Castro *et al.* 1990; Benz *et al.* 1997; Pasyanos *et al.* 2009; Zhao *et al.* 2013b; Zhao & Mousavi 2018; He *et al.* 2021). There is variability in the Q_{Lg} value anomalies at various frequencies. Hence, Q_{Lg} values for specific frequency bands need to be calculated better to reflect the attenuation characteristics of different geological blocks. We statistically analysed the relationship between the average Q_{Lg} values and frequencies within individual geological blocks in this region. Figs 10(a)–(c) illustrate the Q_{Lg} variations versus the frequency in the Baltic Shield, the passive margins, and the North Sea, and Fig. 10(d) summarizes the Q_{Lg} versus frequency curves for all geological blocks. We found that Q_{Lg} values between 0.4 and 4.0 Hz are more robust than other frequencies in characterizing regional attenuation variations. Therefore, the averaged Q_{Lg} between 0.4 and 4.0 Hz was used here to image the broad-band Q_{Lg} and characterize the crustal attenuation for individual geologic blocks (Fig. 11). The broad-band Q_{Lg} maps also have distinct lateral variations and are closely related to regional tectonics. To explore the frequency dependence of crustal Lg attenuation, we further used the power-law model $Q(f) = Q_0 f^{\eta}$ to fit $Q(f)$ between 0.4 and 4.0 Hz and investigate Q_0 (1 Hz Q) and the frequency dependence parameter η. The average Q_0 values are higher in stable regions, such as 583 in the Scandinavian Peninsula and 616 in the Baltic Shield, compared to those in the continental margins and basin areas, which include 397 in the passive margins, 308 in the North Sea and 305 in the Central European Plain. The resulting power-law indexes η range from 0.10 to 0.43 (Table 1), indicating a negative correlation with the Q_0 values (Fig. S4, Supporting Information).

Low Q_{Lg} values can be observed in all three passive margins, in strong contrast to the high Q_{Lg} values seen in the continental region of the Scandinavian Peninsula (profiles c–e in Fig. 11). It can be observed that the crustal thickness increases gradually from the continental margin to the continental region of the peninsula, indicating that the strong variation in Q_{Lg} is related to the changes in crustal thickness. Extremely low Q_{Lg} are observed directly beneath the central North Sea graben and the Central European Plain, possibly due to *Lg*-wave scattering in the graben structure, crustal thinning and sediment cover (profiles a and b in Fig. 11). Higher Q_{Lg} values are observed in stable regions with thicker crust, for example, beneath the continental Scandinavian and Baltic shields. Still, moderate seismicity in this area may challenge the stability of these blocks (profiles a–e in Fig. 11).

4.3. Uncertainty analysis of Q_{Lg} model

To further determine the stability of the system, we used the Bootstrap technique (Efron 1983) for testing. In the inversion calculation, we randomly select 80 per cent of the rays from the total data set, which comprises both single- and two-station data, for inversion to determine the Q_{Lg} value. Then, we repeat the above calculation process 100 times to create 100 new data sets. At 58 independent frequencies, we calculate the mean and relative standard deviation of each point in the region after 100 inversions to quantify the uncertainty of the Q_{Lg} model. The uncertainty results of the Q_{Lg} model for Colombia and its surrounding areas in the active continental margin region show that the Q_{Lg} values inverted using 80 per cent of the randomly selected total data set (Figs 12a and c) are consistent with the results inverted using the complete data set (Figs 9a

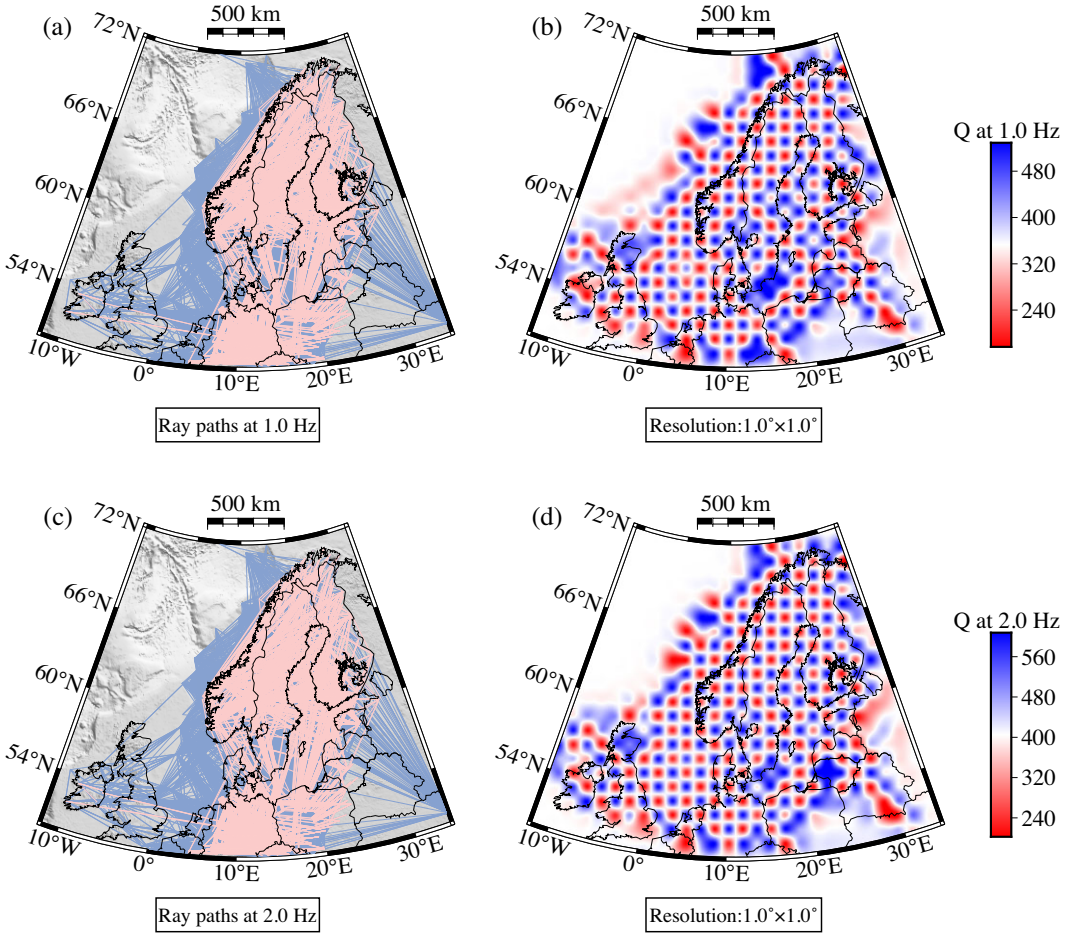

Figure 8. (a) Ray coverage and (b) 1° × 1° checkerboard resolution test at 1.0, where two-station ray paths (pink) are overlapped on the single-station ray paths (blue). (c, d) Similar results for 2.0 Hz.

and c). The relative standard deviation in most regions (Figs 12b and d) is relatively low, with values generally below 20 per cent. Similar to resolution testing, there is significant uncertainty only in the edge areas where the radiation coverage is sparse. This indicates the stability of our data control and inversion system, as well as the high reliability of the Q_{Lg} model.

5 DISCUSSION

5.1. Comparison with previous studies and the cause of Q_{Lg} anomalies

Table 2 compares our Q_{Lg} measurements with existing studies in continental Scandinavia and its marginal regions. In the continental region, Sereno *et al.* (1988) estimated the frequency-dependent *Lg*-wave attenuation and obtained a $Q_0 = 560$ between 1.0 and 7.0 Hz, close to our result of $Q_0 = 544$ in the same band. Dahle *et al.* (1990) established a model of intraplate Q_{Lg} and found a frequency-dependent Q as $Q_{Lg}(f) = 539 + 152f + 1.43f^2$, which has an equivalent $Q_0 = 692$, slightly higher than our result. Alsaker *et al.* (1991) evaluated the efficiency of *Lg* wave propagation and found that the continental Scandinavian features weak attenuation. Kvamme *et al.* (1995) investigated the average Q_{Lg} between 0.2 and 10.0 Hz, obtained an empirical $Q_{Lg}(f) = 440f^{0.7}$, showing a slightly lower attenuation at low frequencies than those from Dahle *et al.* (1990), Sereno *et al.* (1988), and ours of $Q_{Lg}(f) = 585f^{0.11}$.

In the marginal area and shallow sea, Gregersen (1984) found that the North Sea region exhibits strong *Lg*-wave attenuation, attributing it to both thick sediment and subsurface tectonic anomalies. Using explosion data across the central graben in the North Sea, Kennett & Mykkeltveit (1984) observed blockage for *Lg* waves passing through the central graben. Subsequent numerical simulations suggested that faults, complex structures, and thick sediments may impede the efficient passage of *Lg* waves through this area. Mendi *et al.* (1997) simulated the wave propagation in a crust model similar to the North Sea region using a 2-D finite-difference method. They concluded that thin graben structures with high intrinsic attenuation or thick sediments may be responsible for blocking *Lg* waves. Havskov *et al.* (2016) measured the Lg coda Q in the North Sea to investigate variations of coda in different tectonic settings. A coda Q model of $Q_{Coda}(f) = 124f^{0.91}$ was obtained. The strong attenuation in the North Sea region may be attributed to strong scattering caused by the graben structure and thick sediment (Fig. 9d).

Demuth *et al.* (2019) analysed *Lg* wave propagations in Scandinavia and its vicinity. In their tomographic Q maps at 2, 4 and 6 Hz, significant Q_{Lg} variations, from high Q_{Lg} in the Baltic Shield to low Q_{Lg} in the passive margin and North Sea Basin, were likely related to abrupt changes in crust structure and thick sediments (Fig. 9). These attenuation distributions also correspond to lateral changes in crustal mean V_P (Artemieva & Thybo 2013).

Comparing the resulting Lg attenuation with that in the Scandinavian Peninsula and its vicinity, the general distribution trend

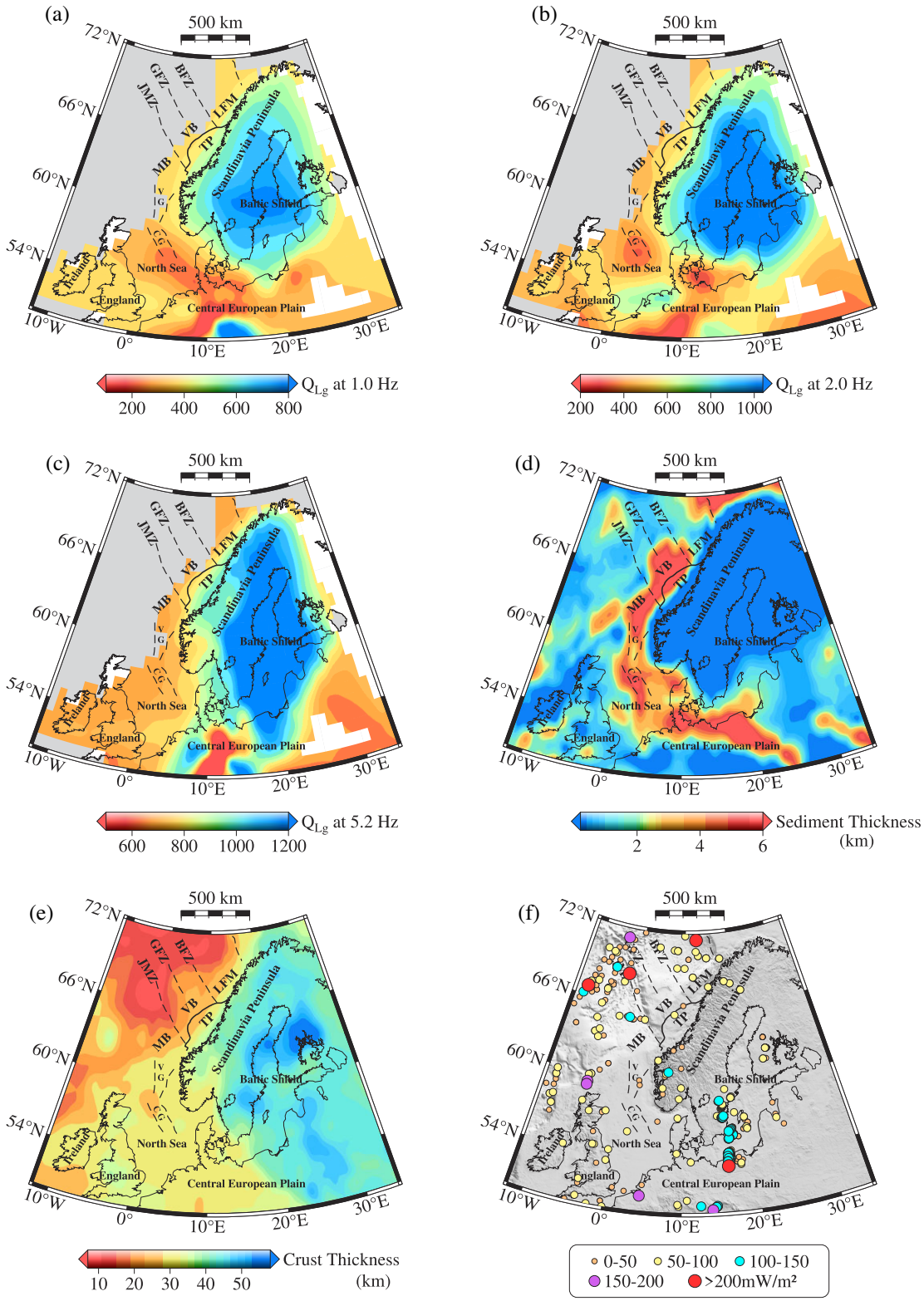

Figure 9. Q_{Lg} maps at 0.5 (a), 1.0 (b) and 2.0 Hz (c), respectively. Note that colour scales vary at different frequencies. The attenuations are also compared with sediment thickness (d) and crust thickness (e), extracted from the CRUST1.0 model (Laske *et al.* 2013), and surface heat flow (f) from the International Heat Flow Commission (IHFC) (Fuchs *et al.* 2021).

and range of Q_{Lg} are consistent, demonstrating the reliability of our result (Table 2). However, by leveraging the larger dataset and the inversion method that combines both single- and two-station data, we achieved significant improvements in the resolution of the Q_{Lg} model. Such a model permits us to link fine-scale attenuation characteristics to geological structures and further investigate their tectonic implications in the Scandinavian Peninsula and its surrounding region.

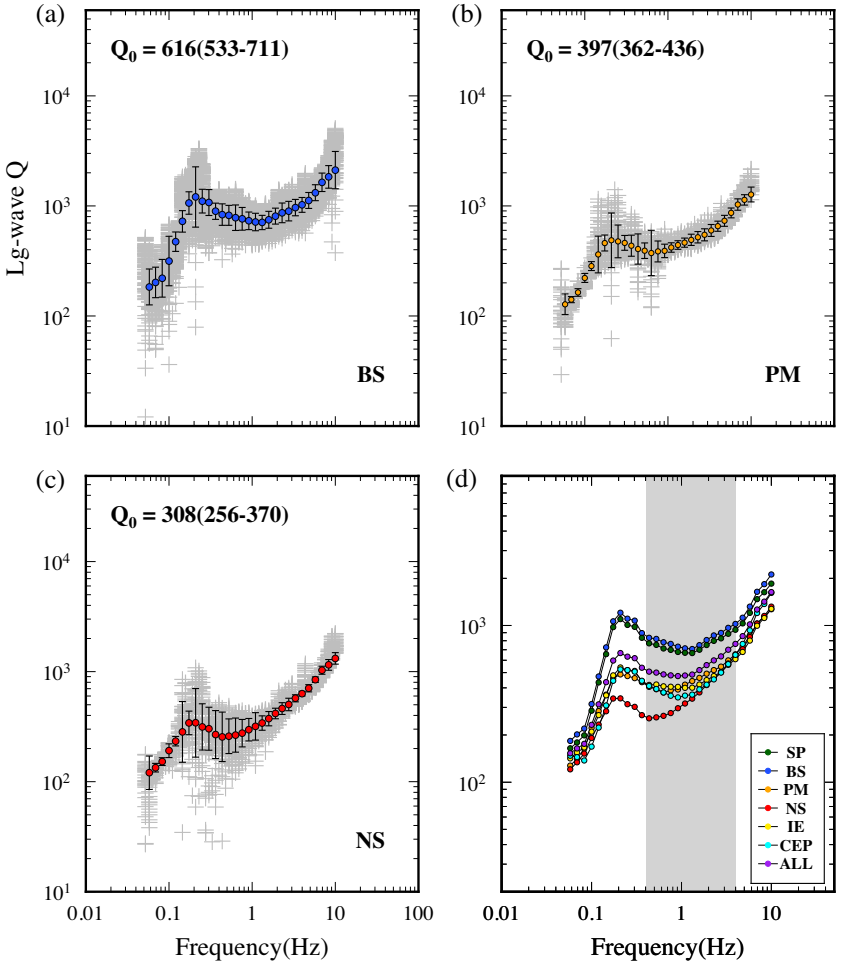

Figure 10. (a–c) Frequency-dependent Q_{Lg} for the Baltic Shield (BS), the passive margin (PM) and the North Sea (NS). The grey crosses are directly observed Q_{Lg} values, and circles and error bars are means and standard deviations at individual frequencies, where circles with different colours represent different regions. (d) Mean Q_{Lg} versus frequency for all geological blocks (Table 1).

5.2 The ancient cratonic core beneath the Baltic Shield

The continental crust of the Baltic Shield formed at approximately 3.5–1.5 Ga (Gaál & Gorbatschev 1987; Lahtinen *et al.* 2008). The Baltic Shield has become the most widely distributed area of Precambrian rocks on the European continent, covering Scandinavia, Finland, northwestern Russia, and the surrounding Baltic Sea (Gorbatschev & Bogdanova 1993). Undergoing multistage tectonic evolution, the margins of the Baltic Shield were disrupted, and the extent of its structurally stable, high-rheological-strength craton crust contracted. For instance, the Early Paleozoic closure of the Iapetus Ocean led to the collision of the Baltic landmass and Laurentia, forming a 3000 km-long Caledonian orogen (Roberts 2003). This collision resulted in intense deformation along the northwestern margin of the Baltic Shield, characterized by deep metamorphism in the thrust structures that formed the proto-Scandinavian Mountains (Fossen 2010). The Caledonian orogen in southern Norway exhibits low Q_{Lg} values, low velocities in the crust, and high-surface heat flow (Figs 9 and 11), which may result from the potential partial melting in the lower crust remaining in the post-collisional extensional environment, reflecting the lower rheological strength in this region (Artemieva 2007; Medhus *et al.* 2012; Artemieva & Thybo 2013; Rickers *et al.* 2013). This orogeny, together with the Carboniferous Variscan orogeny, shaped the basement of the North Sea Basin at the southwestern margin of the Baltic Shield (Ziegler 1990). Influenced by the initial Mesozoic rifting of the North Atlantic, the North Sea underwent several extensional phases, producing a series of grabens typified by the Viking and Central grabens (Ziegler 1975). The uplift of the Jurassic Kimmeridge mantle plume led to extensive crustal uplift in the North Sea Basin, accelerated rates of rift subsidence, and developed deep-water sediment, organic-rich Kimmeridge Clay, and Draupne Formation shales that serve as the main hydrocarbon source rocks (Underhill & Partington 1993; Copestake & Partington 2023). The strong scattering effect of thin crust, thick sedimentation, and graben structure superimposed makes the North Sea basin the area with the lowest Q_{Lg} values (Figs 9 and 11, Table 1). Spatial overlap between the distribution of hydrocarbon source rocks and low Q_{Lg} zones suggests potential links between strong attenuation in passive margin basins and hydrocarbon accumulation (Evans *et al.* 2003). During the Cenozoic, the complete opening of the North Atlantic and the intensification of the Iceland plume caused renewed uplift of the western North Sea and the formation of three passive continental margins—Vøring, Møre and Lofoten-Vesterålen—along the west edge of the Baltic Shield (Anell *et al.* 2009; Patruno *et al.* 2022). Influenced by the Icelandic mantle column, the three passive continental margins underwent extensive magmatism during their

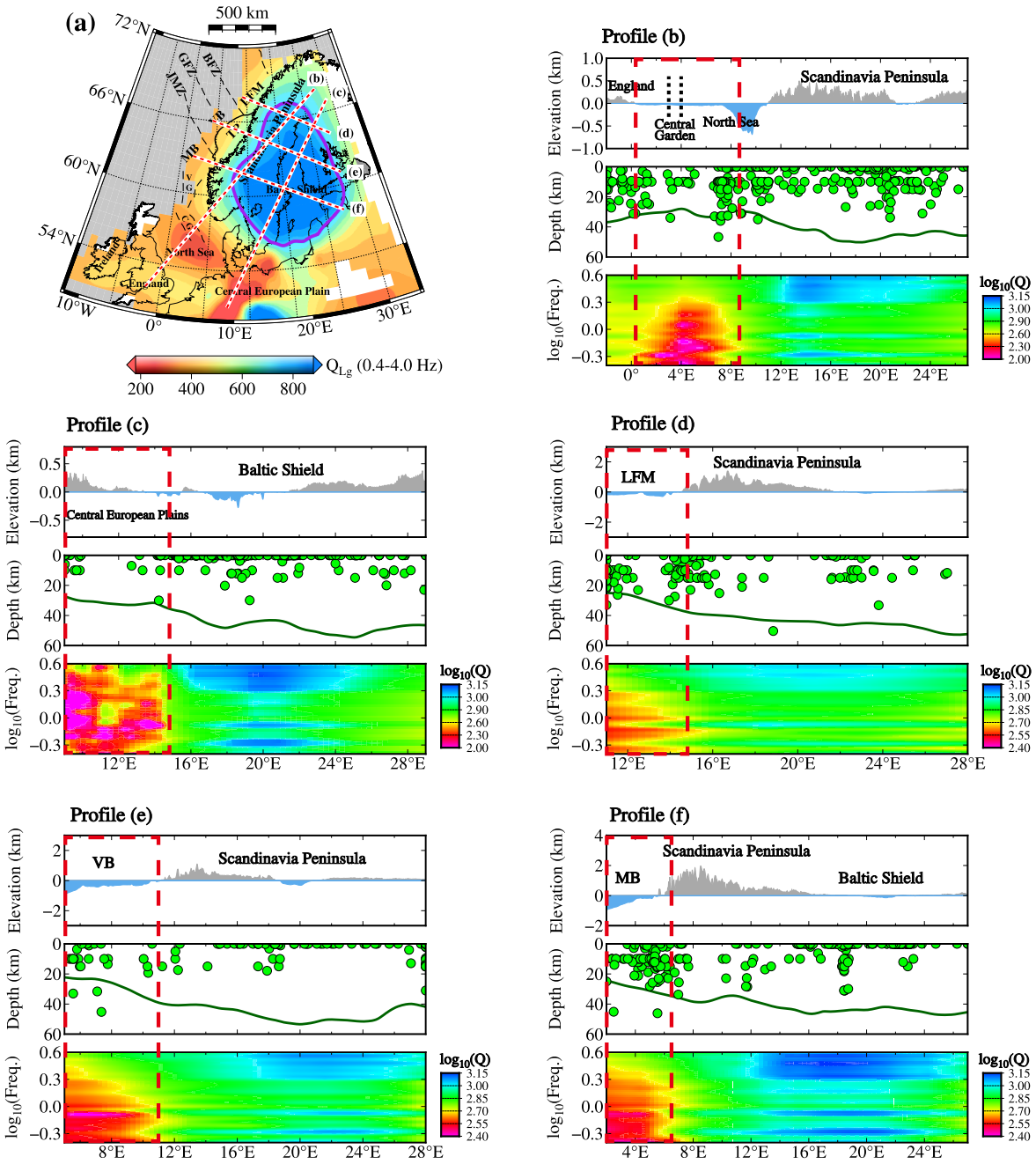

Figure 11. Map showing the broad-band Q_{Lg} averaged between 0.4 and 4.0 Hz (upper left). Overlapped on the map are the surface locations of five Q_{Lg} versus frequency sections (dashed red lines labelled a–e). The rest of the figures (a–e) show these sections. Each of them consists of three subplots: surface topography (top), crustal thickness and seismicity (middle) and profile of Q_{Lg} versus the frequency (bottom). The crust thickness was extracted from the CRUST1.0 model (Laske *et al.* 2013). The purple contour line in Fig. 11(a) circles the cratonic core of the Baltic Shield. The abbreviations are the same as those in Fig. 1.

formation and evolutionary phases, with thick sedimentary cover at the surface and bitter olivine basalts with seaward tilted reflection features in the thin crust, which exhibits strong attenuation characteristics (Figs 9 and 11), reflecting the low-rheological strength nature of the passive margins (Vink 1984; Skogseid *et al.* 2000; Mjelde 2005; Breivik *et al.* 2009; Howell *et al.* 2014; Franke *et al.* 2019). Consequently, the strong tectonic activity of the margins around the Baltic Shield led to the destruction of the ancient Craton crust.

However, geochemical and geological studies indicate that while the margins of the Baltic Shield were affected by collisional and/or orogenic events, its core remained largely intact (Torsvik *et al.* 1996; Roberts 2003; Fossen 2010). The continental part of the Baltic Shield can be divided into two regions based on geochronology: (1) the northeastern Archean domain, comprising gneiss-greenstone belts in northeastern Finland and northwestern Russia (~3.2–2.5 Ga), overlain by Paleoproterozoic sediments on the Archean basement and the Paleoproterozoic Lapland granulite belt (~2.5–1.9

Table 1. Q_{Lg} for individual geological blocks.

Geological block		Q_{Lg} model			CRUST1.0 model[a]	IHFC[b]
Block name	Abbr.	Q_0 (1 Hz Q)	η (0.4–4.0 Hz)	Average Q (0.4–4.0 Hz)	Crustal thickness (km)	Heat flow (mW m^{-2})
Scandinavian Peninsula	SP	585 (503–679)	0.11 ± 0.01	733 (586–916)	40.95 ± 4.64	69.18 ± 20.49
Baltic Shield	BS	616 (533–711)	0.10 ± 0.01	793 (626–1004)	43.78 ± 4.98	60.14 ± 25.40
Passive Continental Margin	PCM	397 (362–436)	0.25 ± 0.02	448 (351–572)	21.43 ± 7.01	60.21 ± 20.94
North Sea	NS	308 (256–370)	0.43 ± 0.03	358 (246–521)	26.46 ± 2.65	42.80 ± 17.44
Ireland–England	IE	367 (353–383)	0.15 ± 0.01	437 (372–514)	31.56 ± 2.42	54.09 ± 20.59
Central European Plain	CEP	305 (210–443)	0.20 ± 0.02	407 (255–452)	35.28 ± 7.22	98.03 ± 97.15
All Areas	AS	428 (302–605)	0.18 ± 0.01	533 (346–821)	37.47 ± 8.43	69.89 ± 49.95

[a]From Laske *et al.* (2013).
[b]From Fuchs *et al.* (2021)

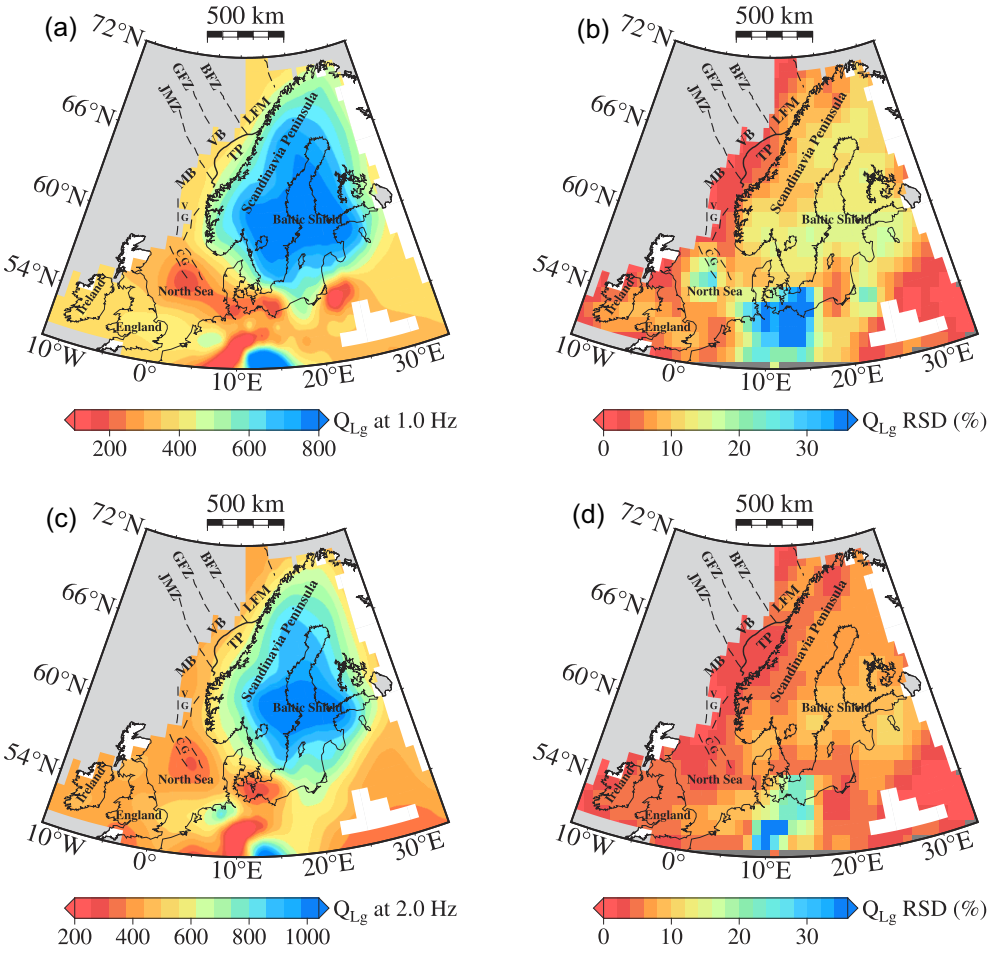

Figure 12. The Q_{Lg} images (left column) obtained through the bootstrap method at 1.0 Hz (a and b) and 2.0 Hz (c and d), and the relative standard deviation distribution for Q_{Lg} model uncertainty (right column).

Ga); and (2) the southern and western Proterozoic domains, including the Svecofennian (∼1.95–1.75 Ga), Sveconorwegian (∼1.1–0.9 Ga), and Trans-Scandinavian Igneous Belt (∼1.85–1.65 Ga) (Artemieva *et al.* 2006; Bogdanova *et al.* 2008). Whether the submarine crust beneath the Baltic Sea belongs to this ancient cratonic block remains uncertain due to the unavailability of surface rock dating, necessitating constraints from deep geophysical data. Typically, ancient cratonic crust is characterized by low tectonic activity, high rheological strength, and low temperatures, resulting in high-seismic velocities and weak seismic attenuation (Pedersen *et al.* 2013; Demuth *et al.* 2019; Paul & Ghosh 2020). Consequently, seismic tomography is an effective tool for delineating the extents of long-lived stable cratonic crust. Compared with seismic velocity, seismic attenuation reflects the anelasticity and scattering characteristics within the Earth's interior, being more sensitive to rheological strength and providing better constraints on the distribution of ancient cratonic crust (Kampfmann & Berckhemer 1985; Mitchell 1995). For example, Shen *et al.* (2023) established a crustal Lg attenuation model for the South China Block, identifying four extremely weak attenuation anomalies that constrain the potential locations of

Table 2. Comparison among different attenuation studies.

Region	Q_0	*Q vs f relation*	Wave type	Number of events	Frequency band (Hz)	Reference
Scandinavia	560	$Q_{Lg}(f) = 560 f^{0.26}$	*Lg*	186	1.0–7.0	Sereno *et al.* 1988
Scandinavia	539	$Q_{Lg}(f) = 539 + 152 f + 1.43 f^2$	*Lg*	87	–	Dahle *et al.* 1990
Scandinavia	–	weak attenuation	*Lg*	195	–	Alsaker *et al.* 1991
Scandinavia	440	$Q_{Lg}(f) = 440 f^{0.7}$	*Lg*	151	0.2–10.0	Kvamme *et al.* 1995
The North Sea	–	Strong attenuation	*Lg*	–	–	Gregersen 1984
The North Sea	–	Strong attenuation	*Lg*	–	–	Kennet & Mykkeltveit 1984
The North Sea	–	Strong attenuation	*Lg*	–	–	Mendi *et al.* 1997
The North Sea	124	$Q_{Coda}(f) = 124 f^{0.91}$	*Coda*	14	–	Havskov *et al.* 2016
Scandinavia and its vicinity	–	Q tomography	*Lg*	279	2.0, 4.0, 6.0	Demuth et al., 2019
Scandinavia	585	$Q_{Lg}(f) = 585 f^{0.38}$	*Lg*	233	1.0–7.0	This study
Scandinavia	585	$Q_{Lg}(f) = 585 f^{0.13}$	*Lg*	233	0.2–10.0	
Scandinavia and its vicinity	–	Q tomography	*Lg*	233	0.05–10.0	

ancient continental relics in the crust. By integrating our crustal Lg attenuation model with other geological and geophysical data, we delineated the extent of ancient cratonic crust in the Scandinavian Peninsula and its surrounding areas. The Baltic Shield, characterized by a dense ray distribution, high-resolution and reliable inversion results, is confined to our study area, which includes only the Scandinavian Peninsula, southwestern Finland, and the Baltic Sea region. The shield blocks exhibit thick crust, high Q_{Lg} values (Figs 9 and 11), and high lithospheric V_{SV}, reflecting their long-term tectonic stability and high-rheological strength (Bogdanova *et al.* 2008; Pedersen *et al.* 2013). Detrital zircon dating studies in this area have found that some sediments are derived from the Archean Craton in the northeast (Huhma and Meriläinen 1991). Eastern peninsula granites yield ages of 1.95 Ga, while southern Finland's tonalitic gneisses date to 1.93–1.92 Ga (Wasström 1993; Lahtinen 1994). Nd–Pb isotopic and geochemical data further confirm 1.9 Ga Paleoproterozoic crust in southern Finland (Lahtinen & Huhma 1997). Thus, the high rheological strength of this region originates from subduction-collision processes during the Proterozoic Svecofennian orogeny, where high-temperature and high-pressure metamorphism, as well as granitic intrusions, shaped the rigid basement of the shield (Gorbatschev & Bogdanova 1993; Lahtinen *et al.* 2005). The purple contour line in Fig. 11(a) shows that the extremely high Q_{Lg} region, where the northern part of the Baltic Sea is involved, is likely the cratonic core of the Baltic Shield. Beneath the cratonic core, a thick cratonic root can be well-constrained based on both velocity tomography and conductivity measurements (Korja *et al.* 1993; Bruneton *et al.* 2004; Sandoval *et al.* 2004; Debayle & Ricard 2012; Pedersen *et al.* 2013).

6 CONCLUSION

Based on broad-band regional seismic data and an inversion method combining both single- and two-station data sets, we developed a high-resolution broad-band *Lg*-wave attenuation model for the Scandinavian Peninsula and its surrounding area, with its frequency band spanning 0.05 to 10.0 Hz, and the spatial resolution reaches approximately 110 km (∼1°). The lateral variation of the Q_{Lg} correlates well with the regional tectonics. These results are consistent with previous studies. However, the high-resolution and wide frequency band of the new Q_{Lg} model enable the investigation of regional tectonic activities on a finer scale and the search for their underlying attenuation mechanisms through frequency-dependent phenomena. The statistically obtained Q_{Lg} versus frequency relations for individual blocks provide additional information for characterizing regional tectonics. Combined with the regional tectonic background, the exceptionally high Q in the Baltic Shield confirms its stability as a Precambrian Craton (Gorbatschev & Bogdanova 1993). The relatively low Q_{Lg} in the core of the Caledonian orogenic belt in southwestern Norway appears to be associated with areas that contain partial melting residuals in the lower crust, induced by post-collisional stretching (Fossen 2010). The combined effect of residual magmatic intrusion, variable crustal thickness, and thick sediments may result in significant Lg attenuation in the volcanic passive continental margins of western Scandinavia. The low Q_{Lg} of the North Sea basin may be related to the crustal thinning, thick sediments, and graben-induced scattering effects. The spatial overlap of low Q_{Lg} areas with hydrocarbon source rocks in the North Sea Basin suggests that strong attenuation zones in continental margin basins may indirectly indicate hydrocarbon-rich areas (Evans *et al.* 2003). The ancient cratonic crust of the undamaged Baltic Shield has been delineated based on extremely high Q_{Lg} values.

ACKNOWLEDGMENTS

We thank Editor Dr E. Bozdag, Assistant Editor F. Storey, reviewer Prof. S. Pei and an anonymous reviewer for their valuable comments, which greatly improved the manuscript. This research was supported by the National Natural Science Foundation of China (U2139206 and 42430306).

SUPPORTING INFORMATION

Supplementary data are available at *GJIRAS* online.

Figure S1. Maps and waveforms showing the ray paths from earthquakes to selected stations and vertical-component velocity seismograms filtered between 0.5 and 5.0 Hz, where (a) and (b) are for the earthquake (pentagon) on 2020 May 18 and (c) and (d) the 2016 October 9 earthquake. The *Lg* waves are highlighted (red), and the code, station name and epicentre distance are labelled.

Figure S2. Site responses at all 560 stations at 0.5 and 1.0 Hz, respectively.

Figure S3. The inverted *Lg* source spectra (green crosses), the best-fitting ω^2 source models (black lines), and the corresponding standard deviation (grey shades) for four earthquakes (a–d). The magnitude m_b, the resultant seismic moment M_0 and the corner frequency f_c are also labelled.

Figure S4. (a) Example of calculating η. (b) The lateral distribution of the frequency dependence parameter η.

Table S1. Earthquake parameters used in this study
Table S2. Station parameters used in this study.
Table S3. Networks used in this study

Please note: Oxford University Press are not responsible for the content or functionality of any supporting materials supplied by the authors. Any queries (other than missing material) should be directed to the corresponding author for the article.

DATA AVAILABILITY

Waveform and station metadata were downloaded using Obspy (Krischer *et al*. 2015) through the International Federation of Digital Seismograph Networks (FDSN) webservices and obtained from the GEOFON Data Management Center at https://geofon.gfz-potsdam.de/waveform/archive/(last accessed October 2024) and Incorporated Research Institutions for Seismology Data Management Center (IRISDMC) at http://www.iris.edu/ds/nodes/dmc/(last accessed October 2024), and the associated network operators are listed in Table S2 (Supporting Information). Many waveform data are contributed to the GEOFON and IRIS by local or international seismic networks, for instance, the Swedish National Seismological Network (SNSN). Names of all networks used in this study are listed in Table S3 (Supporting Information). The single- and two-station Lg amplitude data used in this study and the resulting *Lg*-wave attenuation model in the Scandinavian Peninsula and its vicinity can be accessed on the World Data Centre for Geophysics, Beijing (WDCGB) at https://doi.org/10.12197/2022GA034 (last accessed October 2024). Certain figures were generated using Generic Mapping Tools (GMT) at https://www.generic-mapping-tools.org/(last accessed October 2024) (Wessel *et al.* 2019).

REFERENCES

Aki, K. & Chouet, B., 1975. Origin of coda waves: source, attenuation and scattering effects, *J. Geophys. Res.,* **80,** 3322–3342.

Alsaker, A., Kvamme, L., Hansen, R., Dahle, A. & Bungum, H., 1991. The M_L scale in Norway, *Bull. seism. Soc. Am.,* **81,** 379–398.

Anell, I., Thybo, H. & Artemieva, I.M., 2009. Cenozoic uplift and subsidence in the North Atlantic region: geological evidence revisited, *Tectonophysics,* **474,** 78–105.

Artemieva, I.M., 2007. Dynamic topography of the East European craton: shedding light upon lithospheric structure, composition and mantle dynamics, *Global Planet. Change,* **58,** 411–434.

Artemieva, I.M. & Shulgin, A., 2019. Making and altering the crust: a global perspective on crustal structure and evolution, *Earth planet. Sci. Lett.,* **512,** 8–16.

Artemieva, I.M. & Thybo, H., 2013. EUNAseis: a seismic model for Moho and crustal structure in Europe, Greenland, and the North Atlantic region, *Tectonophysics,* **609,** 97–153.

Artemieva, I.M., Thybo, H. & Kaban, M.K., 2006. Deep Europe today: geophysical synthesis of the upper mantle structure and lithospheric processes over 3.5 Ga, *Geological Society, London, Memoirs,* **32,** 11–41.

Benz, H.M., Frankel, A. & Boore, D.M., 1997. Regional Lg attenuation for the continental United States, *Bull. seism. Soc. Am.,* **87,** 606–619.

Blystad, P., Brekke, H., Frseth, R.B., Larsen, B.T. & Trudbakken, B., 1995. Structural elements of the Norwegian continental shelf. Part 2. The Norwegian Sea region, The Norwegian Petroleum Directorate.

Bogdanova, S.V., Bingen, B., Gorbatschev, R., Kheraskova, T.N., Kozlov, V.I., Puchkov, V.N. & Volozh, Y.A., 2008. The East European Craton (Baltica) before and during the assembly of Rodinia, *Precambrian Res.,* **160,** 23–45.

Bouchon, M., 1982. The complete synthesis of seismic crustal phases at regional distances, *J. geophys. Res.,* **87,** 1735–1741.

Breivik, A.J., Faleide, J.I., Mjelde, R. & Flueh, E.R., 2009. Magma productivity and early seafloor spreading rate correlation on the northern Vøring Margin, Norway—constraints on mantle melting, *Tectonophysics,* **468,** 206–223.

Bruneton, M. *et al.*, 2004. Complex lithospheric structure under the central Baltic Shield from surface wave tomography -: art. No. B10303, *J. Geophys. Res. Solid Earth,* **109**.

Bukovics, C., Cartier, E.G., Shaw, N.D. & Ziegler, P.A., 1984. Structure and development of the mid-Norway continental margin, In: *Petroleum Geology of the North European Margin,* ed., Spencer, A.M., Springer, Dordrecht.

Campillo, M., Feignier, B., Bouchon, M. & Bethoux, N., 1993. Attenuation of crustal waves across the Alpine Range, *J. geophys. Res.,* **98,** 1987–1996.

Campillo, M. & Plantet, J.L., 1991. Frequency-dependence and spatial-distribution of seismic attenuation in France—experimental results and possible interpretations, *Phys. Earth planet. Inter.,* **67,** 48–64.

Castro, R.R., Anderson, J.G. & Singh, S.K., 1990. Site response, attenuation and source spectra of S-waves along the Guerrero, Mexico, subduction zone, *Bull. seism. Soc. Am.,* **80,** 1481–1503.

Copestake, P. & Partington, M.A., 2023. *Sequence Stratigraphy of the Jurassic–lowermost Cretaceous (Hettangian–Berriasian) of the North Sea Region*. Geological Society of London.

Dahle, A., Bungum, H. & Kvamme, L.B., 1990. Attenuation models inferred from intraplate earthquake recordings, *Earthq. Eng. Struct. Dyn.,* **19,** 1125–1141.

Debayle, E. & Ricard, Y., 2012. A global shear velocity model of the upper mantle from fundamental and higher Rayleigh mode measurements, *J. Geophys. Res. Solid Earth,* **117**.

Demuth, A., Ottemller, L. & Keers, H., 2019. QLg wave tomography beneath Norway, *J. Seismol.,* **23,** 151–164.

Efron, B., 1983. Estimating the error rate of a prediction rule—improvement on cross-validation, *J. Am. Stat. Assoc.,* **78,** 316–331.

Erickson, D., McNamara, D.E. & Benz, H.M., 2004. Frequency-dependent Lg Q within the continental United States, *Bull. seism. Soc. Am.,* **94,** 1630–1643.

Evans, D., Graham,, C., Armour,, A. & Bathurst,, P., 2003. The millennium atlas : petroleum geology of the central and northern North Sea. The Geological Society of London.

Faleide, J.I., Bjorlykke, K. & Gabrielsen, R.H., 2010. Geology of the Norwegian continental shelf, *Petroleum Geoscience*. Springer, Berlin, Heidelberg, pp.467–469.

Faleide, J.I., Tsikalas, F., Breivik, A.J., Mjelde, R., Ritzmann, O., Engen, O., Wilson, J. & Eldholm, O., 2008. Structure and evolution of the continental margin off Norway and Barents Sea, *Episodes,* **31,** 82–91.

Fan, G.W. & Lay, T., 2003. Strong Lg wave attenuation in the northern and eastern Tibetan Plateau measured by a two-station/two-event stacking method, *Geophys. Res. Lett.,* **30**.

Fossen, H., 2010. Extensional tectonics in the North Atlantic Caledonides: a regional view, *Geological Society, London, Special Publications,* **335,** 767–793.

Franke, D. *et al.* 2019. Polyphase magmatism during the formation of the Northern East Greenland continental margin, *Tectonics,* **38,** 2961–2982.

Fuchs, S., Norden, B., Artemieva, I., Chiozzi, P. & Verdoya, M., 2021. *The Global Heat Flow Database: Release 2021*. GFZ Data Services.

Furumura, T. & Kennett, B.L.N., 1997. On the nature of regional seismic phases-II. On the influence of structural barriers, *Geophys. J. Int.,* **129,** 221–234.

Gaál, G. & Gorbatschev, R., 1987. An outline of the precambrian evolution of the Baltic Shield, *Precambrian Res.,* **35,** 15–52.

Gorbatschev, R. & Bogdanova, S., 1993. Frontiers in the Baltic Shield, *Precambrian Res.,* **64,** 3–21.

Gregersen, S., 1984. Lg-wave propagation and crustal structure differences near Denmark and the North Sea, *Geophys. J. Int.,* **79,** 217–234.

Gutenberg, B., 1955. Channel waves in the earth's crust, *Geophysics,* **20,** 283–294.

Hasegawa, H.S., 1985. Attenuation of Lg waves in the Canadian Shield, *Bull. seism. Soc. Am.,* **75,** 1569–1582.

Havskov, J., Sorensen, M.B., Vales, D., Ozyazicioglu, M., Sanchez, G. & Li, B., 2016. Coda Q in different tectonic areas, influence of processing parameters, *Bull. seism. Soc. Am.,* **106,** 956–970.

He, X., Zhao, L.F., Xie, X.B., Tian, X. & Yao, Z.X., 2021. Weak crust in southeast Tibetan plateau revealed by Lg-wave attenuation tomography: implications for crustal material escape, *J. Geophys. Res.,* **126,** e2020JB020748.

Herrmann, R.B. & Kijko, A., 1983. Short-period Lg magnitudes-instrument, attenuation, and source effects, *Bull. seism. Soc. Am.,* **73,** 1835–1850.

Howell, S.M., Ito, G., Breivik, A.J., Rai, A., Mjelde, R., Hanan, B., Sayit, K. & Vogt, P., 2014. The origin of the asymmetry in the Iceland hotspot along the Mid-Atlantic Ridge from continental breakup to present-day, *Earth planet. Sci. Lett.,* **392,** 143–153.

Huhma, H. & Meriläinen, K., 1991. Provenance of paragneisses from the Lapland granulite belt, In: *Metamorphism, Deformation and Structure of the Crust, abstracts (IGCP 275),* pp. 26, eds, Tuisku, P. & Laajoki, K., Res Terrae, Series A.

Kampfmann, W. & Berckhemer, H., 1985. High-temperature experiments on the elastic and anelastic behaviour of magmatic rocks, *Phys. Earth planet. Inter.,* **40,** 223–247.

Kennett, B.L.N., 1986. Lg-waves and structural boundaries, *Bull. seism. Soc. Am.,* **76,** 1133–1141.

Kennett, B.L.N. & Mykkeltveit, S.M., 1984. Guided-waves in laterally varying media-the Lg phase in the North-Sea basin, *Geophys. J. R. Astron. Soc.,* **77,** 302–302.

Knopoff, L., Schwab, F. & Kauselt, E., 1973. Interpretation of Lg, *Geophys. J. Int.,* **33,** 389–404.

Korja, A., Korja, T., Luosto, U. & Heikkinen, P., 1993. Seismic and geoelectric evidence for collisional and extensional events in the Fennoscandian Shield—implications for precambrian crustal evolution, *Tectonophysics,* **219,** 129–152.

Krischer, L., Megies, T., Barsch, R., Beyreuther, M., Lecocq, T., Caudron, C. & Wassermann, J., 2015. ObsPy: A bridge for seismology into the scientific Python ecosystem, *Comput. Sci. Discov.,* **8**(1), 014003.

Kvamme, L., Hansen, R. & Bungum, H., 1995. Seismic-source and wave-propagation effect of Lg waves in Scandinavia, *Geophys. J. Int.,* **120,** 525–536.

Kvarven, T., Mjelde, R., Hjelstuen, B.O., Faleide, J.I., Thybo, H., Flueh, E.R. & Murai, Y., 2016. Crustal composition of the Møre Margin and compilation of a conjugate Atlantic margin transect, *Tectonophysics,* **666,** 144–157.

Lahtinen, R., 1994. Crustal evolution of the svecofennian and Karelian domains during 2.1-1.79 Ga, with special emphasis on the geochemistry and origin of 1.93-1.91 Ga gneissic tonalites and associated supracrustal rocks in the Rautalampi area, central Finland, *Geol. Surv. Finl. Bull.,* **378,** 128.

Lahtinen, R., Garde, A.A. & Melezhik, V.A., 2008. Paleoproterozoic evolution of Fennoscandia and Greenland, *Episodes,* **31,** 20–28.

Lahtinen, R. & Huhma, H., 1997. Isotopic and geochemical constraints on the evolution of the 1.93-1.79 Ga svecofennian crust and mantle in Finland, *Precambrian Res.,* **82,** 13–34.

Lahtinen, R., Korja, A. & Nironen, M., 2005. Chapter 11 paleoproterozoic tectonic evolution, in: *Developments in Precambrian Geology,* pp. 481–531, eds, Lehtinen, M., Nurmi, P.A. & Rämö, O.T., Elsevier.

Laske, G., Masters, G., Ma, Z. & Pasyanos, M., 2013. Update on CRUST1.0–A 1-degree global model of earth's crust, *EGU General Assembly Conference,* Vienna, Austria, EGU2013–2658.

Luo, Y., Zhao, L.F., Ge, Z.X., Xie, X.B. & Yao, Z.X., 2021. Crustal Lg-wave attenuation in Southeast Asia and its implications for regional tectonic evolution, *Geophys. J. Int.,* **226,** 1873–1884.

Ma, X., Zhao, L.F., Xie, X.B., Chang, X. & Yao, Z.X., 2023. Warm versus cold crust in the Tien Shan orogenic belt revealed by seismic Lg attenuation tomography, *Geophys. J. Int.,* **233,** 2142–2154.

Medhus, A.B., Balling, N., Jacobsen, B.H., Weidle, C., England, R.W., Kind, R., Thybo, H. & Voss, P., 2012. Upper-mantle structure beneath the Southern Scandes Mountains and the Northern Tornquist Zone revealed by P-wave traveltime tomography, *Geophys. J. Int.,* **189,** 1315–1334.

Mendi, C.D., Ruud, B.O. & Husebye, E.S., 1997. The North Sea Lg-blockage puzzle, *Geophys. J. Int.,* **130,** 669–680.

Mitchell, B.J., 1995. Anelastic structure and evolution of the continental-crust and upper-mantle from seismic surface-wave attenuation, *Rev. Geophys.,* **33,** 441–462.

Mjelde, R., 2005. Continent-ocean transition on the Vøring Plateau, NE Atlantic, derived from densely sampled ocean bottom seismometer data, *J. geophys. Res.* **110**.

Mosar, J., 2003. Scandinavia's North Atlantic passive margin, *J. geophys. Res.,* **108**.

Ottemöller, L., Shapiro, N.M., Singh, S.K. & Pacheco, J.F., 2002. Lateral variation of Lg wave propagation in southern Mexico, *J. geophys. Res.,* **107,** ESE 3–1-ESE 3-13.

Paige, C.C. & Saunders, M.A., 1982. Lsqr: an algorithm for sparse linear-equations and sparse least-squares, *ACM Trans. Math. Softw.,* **8,** 43–71.

Pasyanos, M., Matzel, E., Walter, W. & Rodgers, A., 2009. Broad-band Lg attenuation modelling in the Middle East, *Geophys. J. Int.,* **177,** 1166–1176.

Patruno, S., Kombrink, H. & Archer, S.G., 2022. Cross-border stratigraphy of the Northern, Central and Southern North Sea: a comparative tectono-stratigraphic megasequence synthesis, *Geol. Soc. London Spec. Publ.,* **494,** 13–83.

Paul, J. & Ghosh, A., 2020. Evolution of cratons through the ages: a time-dependent study, *Earth planet. Sci. Lett.,* **531,** 115 962.

Pedersen, H.A., Debayle, E. & Maupin, V., 2013. Strong lateral variations of lithospheric mantle beneath cratons—example from the Baltic Shield, *Earth planet. Sci. Lett.,* **383,** 164–172.

Press, F. & Ewing, M., 1952. Two slow surface waves across North America, *Bull. seism. Soc. Am.,* **42,** 219–228.

Rickers, F., Fichtner, A. & Trampert, J., 2013. The Iceland-Jan Mayen plume system and its impact on mantle dynamics in the North Atlantic region: evidence from full-waveform inversion, *Earth planet. Sci. Lett.,* **367,** 39–51.

Roberts, D., 2003. The Scandinavian Caledonides: event chronology, palaeogeographic settings and likely, modern analogues, *Tectonophysics,* **365,** 283–299.

Ruzaikin, A.I., Nersesov, I.L., Khalturin, V.I. & Molnar, P., 1977. Propagation of Lg and lateral variations in crustal structure in Asia, *J. geophys. Res.,* **82,** 307–316.

Sandoval, S., Kissling, E., Ansorge, J. & Work, S.S.T., 2004. High-resolution body wave tomography beneath the SVEKALAPKO array—II. Anomalous upper mantle structure beneath the central Baltic Shield, *Geophys. J. Int.,* **157,** 200–214.

Sato, R., 1967. Attenuation of seismic waves, *J. Phys. Earth,* **15,** 32–61.

Schlittenhardt, J., 2001. Teleseismic Lg of Semipalatinsk and Novaya Zemlya nuclear explosions recorded by the GRF (Grafenberg) array: comparison with regional Lg (BRV) and their potential for accurate yield estimation, *Pure appl. Geophys.,* **158,** 2253–2274.

Sclater, J.G. & Christie, P.A.F., 1980. Continental stretching—an explanation of the post-mid-cretaceous subsidence of the central North-Sea basin, *J. geophys. Res.,* **85,** 3711–3739.

Sereno, T.J., Bratt, S.R. & Bache, T.C., 1988. Simultaneous inversion of regional wave spectra for attenuation and seismic moment in Scandinavia, *J. geophys. Res.,* **93,** 2019–2035.

Shapiro, N., Béthoux, N., Campillo, M. & Paul, A., 1996. Regional seismic phases across the Ligurian Sea: Lg blockage and oceanic propagation, *Phys. Earth planet. Inter.,* **93,** 257–268.

Shen, L., Zhao, L.F., Xie, X.B., Yang, G. & Yao, Z.X., 2023. Extremely weak Lg attenuation reveals ancient continental relicts in the South China block, *Earth planet. Sci. Lett.,* **611,** 118 144.

Singh, S. & Herrmann, R.B., 1983. Regionalization of crustal coda Q in the continental United States, *J. geophys. Res.,* **88,** 527.

Skogseid, J., Planke, S., Faleide, J.I., Pedersen, T., Eldholm, O. & Neverdal, F., 2000. NE Atlantic continental rifting and volcanic margin formation, *Geol. Soc. Lond. Spec. Publ.,* **167,** 295–326.

Smith, W.H.F. & Wessel, P., 1990. Gridding with continuous curvature splines in tension, *Geophysics,* **55,** 293–305.

Street, R.L., Herrmann, R.B. & Nuttli, O.W., 1975. Spectral characteristics of Lg wave generated by central United-States earthquakes, *Geophys. J. R. Astron. Soc.,* **41,** 51.

Tesauro, M., Kaban, M.K. & Cloetingh, S.A.P.L., 2008. EuCRUST-07: a new reference model for the European crust, *Geophys. Res. Lett.,* **35**.

Torsvik, T.H., Smethurst, M.A., Meert, J.G., VanderVoo, R., McKerrow, W.S., Brasier, M.D., Sturt, B.A. & Walderhaug, H.J., 1996. Continental break-up and collision in the neoproterozoic and palaeozoic—A tale of Baltica and Laurentia, *Earth Sci. Rev.,* **40,** 229–258.

Tsikalas, F., Faleide, J.I., Eldholdm, O. & Wilson, J., 2005. Late mesozoic-cenozoic structural and stratigraphic correlations between the conjugate mid-Norway and NE Greenland continental margins, *Geol. Soc. London Petroleum Geol. Conf. Series,* **6,** 785–801.

Underhill, J.R. & Partington, M.A., 1993. Jurassic thermal doming and deflation in the North-Sea—implications of the sequence stratigraphic evidence, *Petroleum Geology of Northwest Europe: Proceedings of the 4th Conference,* Geological Society, London, **4,** 337–345.

Vink, G.E., 1984. A hotspot model for Iceland and the Vøring Plateau, *J. Geophys. Res.,* **89,** 9949–9959.

Wasström, A., 1993. The Knaften granitoids of Västerbotten County, northern Sweden, In: *Radiometric Dating Results,* Vol. **823,** pp. 60–64, ed., Lundqvist, Th., Geol. Surv. Swed. Res. Pap. C.

Wessel, P., Luis, J.F., Uieda, L., Scharroo, R., Wobbe, F., Smith, W.H.F. & Tian, D., 2019. The generic mapping tools version 6, *Geochem. Geophys. Geosyst.,* **20,** 5556–5564.

Wu, R.S., Jin, S. & Xie, X.B., 2000. Energy partition and attenuation of Lg waves by numerical simulations using screen propagators, *Phys. Earth planet. Inter.,* **120,** 227–243.

Xie, J., Gok, R., Ni, J. & Aoki, Y., 2004. Lateral variations of crustal seismic attenuation alongthe INDEPTH profiles in Tibet from Lg Q inversion, *J. Geophys. Res. Solid Earth,* **109,** B10308.

Xie, J., Wu, Z., Liu, R., Schaff, D., Liu, Y. & Liang, J., 2006. Tomographic regionalization of crustal Lg Q in eastern Eurasia, *Geophys. Res. Lett.,* **33**.

Xie, X.B. & Lay, T., 1994. The excitation of Lg waves by explosions: a finite-difference investigation, *Bull. seism. Soc. Am.,* **84,** 324–342.

Yang, G., Chen, L., Zhao, L.F., Xie, X.B. & Yao, Z.X., 2023. Crustal Lg attenuation beneath the Iranian plateau: implications for cenozoic magmatism related to slab subduction, slab break-off, and mantle flow, *J. Geophys. Res. Solid Earth,* **128,** e2022JB025664.

Yoshimoto, K., Sato, H. & Ohtake, M., 1993. Frequency-dependent attenuation of P-wave and S-wave in the Kanto Area, Japan, based on the coda-normalization method, *Geophys. J. Int.,* **114,** 165–174.

Zelt, C.A., 1998. Lateral velocity resolution from three-dimensional seismic refraction data, *Geophys. J. Int.,* **135,** 1101–1112.

Zhang, L., Zhao, L.F., Xie, X.B., Wu, Q.J. & Yao, Z.X., 2022. Lateral variations in crustal Lg attenuation in and around the Hangay Dome, *Mongolia. Int. J. Earth Sci.,* **111,** 591–606.

Zhao, L.F. & Mousavi, S.M., 2018. Lateral variation of crustal Lg attenuation in Eastern North America, *Sci Rep,* **8,** 7285.

Zhao, L.F. & Xie, X.B., 2016. Strong Lg-wave attenuation in the Middle East continental collision orogenic belt, *Tectonophysics,* **674,** 135–146.

Zhao, L.-F., Xie, X.-B., He, J.-K., Tian, X. & Yao, Z.-X., 2013a. Crustal flow pattern beneath the Tibetan Plateau constrained by regional Lg-wave Q tomography, *Earth planet. Sci. Lett.,* **383,** 113–122.

Zhao, L.F., Xie, X.B., Wang, W.M., Zhang, J.H. & Yao, Z.X., 2010. Seismic Lg-wave Q tomography in and around northeast China, *J. Geophys. Res. Solid Earth,* **115,** B08307.

Zhao, L.-F., Xie, X.-B., Wang, W.-M., Zhang, J.-H. & Yao, Z.-X., 2013b. Crustal Lg attenuation within the North China Craton and its surrounding regions, *Geophys. J. Int.,* **195,** 513–531.

Zhou, L.Q., Zhao, C.P., Chen, Z.L. & Zheng, S.H., 2011. Amplitude tomography of lg waves in Xinjiang and its adjacent regions, *Bull. seism. Soc. Am.,* **101,** 1302–1314.

Ziegler, P.A., 1975. Geologic evolution of North Sea and its tectonic Framework1, *AAPG Bull.,* **59,** 1073–1097.

Ziegler, P.A., 1986. Geodynamic model for the palaeozoic crustal consolidation of Western and Central Europe, *Tectonophysics,* **126,** 303–328.

Ziegler, P.A., 1990. *Geological Atlas of Western and Central Europe,* Geological Society of London.

Zor, E., Sandvol, E., Xie, J.K., Turkelli, N., Mitchell, B., Gasanov, A.H. & Yetirmishli, G., 2007. Crustal attenuation within the Turkish plateau and surrounding regions, *Bull. seism. Soc. Am.,* **97,** 151–161.